International Journal of Technology 14(3) 501-509 (2023)
Received August 2022 / Revised October 2022 / Accepted November 2022

International Journal of Technology

http://ijtech.eng.ui.ac.id

$Ca_8MgY(PO_4)_7:Eu^{2+},Mn^{2+}$: A Promising Phosphor in Near-Ultraviolet WLED Devices

My Hanh Nguyen Thi[1], Nguyen Le Thai[2], Thuc Minh Bui[3], Nguyen Thi Phuong Thao[4*]

[1]*Faculty of Mechanical Engineering, Industrial University of Ho Chi Minh City, Ho Chi Minh City, Vietnam*
[2]*Faculty of Engineering and Technology, Nguyen Tat Thanh University, Ho Chi Minh City, Vietnam*
[3]*Faculty of Electrical and Electronics Engineering, Nha Trang University, Nha Trang City, Vietnam*
[4]*Faculty of Electrical and Electronics Engineering, Ton Duc Thang University, Ho Chi Minh City, Vietnam*

Abstract. Through employing the solid-state process under significant temperature, we produced a sequence of single-element radiation-adjustable phosphors $Ca_8MgR(PO_4)_7:Eu^{2+},Mn^{2+}$ or CaMg:EM (R = La, Y), and thoroughly analyzed the crystalline arrangement, photoluminescence (PL), PL excitation (PLE), as well as the degrading period. The findings suggest that $Ca_8MgLa(PO_4)_7:Eu^{2+},Mn^{2+}$ could be a green contender to be used within close ultraviolet-chip white light-emitted diode (WLED) devices. It is possible to change the emitting green hue from $Ca_8MgLa_{1-x}Y_x(PO_4)_7$ treated with Eu^{2+} to cyan by adjusting the La^{3+}/Y^{3+} proportion for the purpose of lowering the crystal field potency. Furthermore, power shift among Eu^{2+} and Mn^{2+} would be used to create a conventional one-stage white CaMg:EM having a CIE hue coordinate shown as (0.330, 0.328). The power transmission process was shown in the form of resonant dipole-quadrupole nature. In addition, we also computed the critical range. The white-emitting single-composition CaMg:EM was effectively coated above one close ultraviolet chip under 375 nm, indicating that it may become a strong choice of phosphor within close ultraviolet WLED devices.

Keywords: Color homogeneity; Double-layer phosphor; Luminous flux; Monte Carlo theory; WLED

1. Introduction

Being used for LCD devices as well as solid-state illumination, white light-emitted diode (WLED) devices have gotten significant academic as well as commercial interest (Yigen *et al.*, 2021; Yu *et al.*, 2021; Liu *et al.*, 2021). In the latest days, the commercialized white LED, which is made by mixing a blue chip of LED with $YAG:Ce^{3+}$ phosphor in yellow, has become a significant part of solid-state illumination (Kumar *et al.*, 2019). This mixture, though, has certain drawbacks, including a poor CRI measured at roughly 70 to 80, as well as a significant CCT measured at 7750 K, caused by a shortage of elements in red (Chen *et al.*, 2019a). Because of their great color-rendering characteristics, WLED devices with three hues may prove effective for improving CRIs (Xia *et al.*, 2019). However, the varied aging rates of each phosphor, as well as the blue illumination's repeating absorptivity via phosphors in green as well as red, would result in small luminous effectiveness in this formation. One-stage phosphors generating illumination in white activated via ultraviolet or close ultraviolet chip may become a decent solution for such difficulties (Adnan *et al.*,

*Corresponding author's email: nguyenthiphuongthao@tdtu.edu.vn, Tel.: +84-09-77362626
doi: 10.14716/ijtech.v14i3.5904

2021; Jen *et al*., 2021; Chen *et al*., 2019b). For the study, we produced multiple CaMg:EM phosphors possessing crystal formation of β-$Ca_3(PO_4)_2$ via the solid-state technique under a significant temperature below a reducing environment: 15% H_2 along with 85% N_2. We produced the usual white one-element phosphor having CIE hue coordinates shown as (0.330, 0.328) by altering the ratios between La^{3+} and Y^{3+}, as well as Eu^{2+} and Mn^{2+} via a hypothesis concerning crystal field potency, as well as power shift in both, whereas past projects concerning associated mixtures concentrated on power shift or achieved illumination in white through combining a pair of phosphor elements (Sun *et al*., 2022; Huu and Thi, 2022; Hakim *et al*., 2021).

Our study examined the brightness characteristics for CaMg:EM and the power conversion between Eu^{2+} and Mn^{2+} within $Ca_8MgY(PO_4)_7$ using PL under excitation wavelengths measured at 334 nm as well as 375 nm, along with the lifetime duration as well as concentration. Eventually, the electroluminescence characteristics of a white LED device were revealed after creating a merger between CaMg:EM and one close ultraviolet chip.

2. Experimental

2.1. Materials characterization

Table 1 Phosphor characteristics and tools used for assessment under room temperature

Characteristics	Tools
Phase purity	X-ray diffractometer, model D-max 2200 from Rigaku (Japan), accompanied by Cu-Kα radiation with a wavelength of 1.5405, under 30 kilovolts as well as 30 milliamperes
PL, PLE, and degradation arches	Edinburgh Instruments FPS 920 Time Resolved and Steady State Fluorescence Spectrometers outfitted with 450-W xenon as well as 150-W nF900 lights

2.2. LED manufacturing

We created the WLEDs by coupling one close ultraviolet chip under 375 nm with the as-yet-unsynthesized phosphors. The gadgets' spectra of EL (short for electroluminescence) were acquired using a spectrophotometer of EVERFINE PMS-80 UV-VIS-IR at room temperature and a direct current of 0.02 A (Dang *et al*., 2020; Orudzhev, Abdullaeva, and Dzhabbarov, 2019; Lin *et al*., 2019).

3. Results and Discussion

The cause for this will be explained more within a segment concerning CaMg:EM. It is possible to estimate the critical spacing among ions of Eu^{2+} by utilizing Blasse's equation (Kaur *et al*., 2020).

The cause for this will be explained more within a segment concerning CaMg:EM. It is possible to estimate the critical spacing among ions of Eu^{2+} by utilizing Blasse's equation (Kaur *et al*., 2020).

$$R_c = 2\left[\frac{3V}{4\pi x_c N}\right]^{\frac{1}{3}} \quad (1)$$

R_c denotes the cleavage among the closest ions of Eu^{2+} under x_c. V denotes the unit-cell volume. N denotes the amount of accessible dopant locations in a cell. x_c indicates the critical concentration.

It is possible to calculate the intensity of the crystal field surrounding Eu^{2+} via a formula (Kim *et al.*, 2019).

$$D_q = \frac{Ze^2r^4}{6R^5} \quad (2)$$

D_q indicates the intensity of the crystal field. Z indicates the anion's valence. r indicates the d wavefunction's radius. e indicates the charge of electron. R indicates the range separating the center ion and ligands. The replacement of lesser Y^{3+} ions for more La^{3+} ions in the latticework of CaMg:EM generates a longer gap extending from Eu^{2+} to O_2 within the latticework of the host, causing a continual rise of the blue-shift for the discharge between green and cyan. Identical phenomena have been observed in $(Ca,Mg,Sr)Y(PO_4)_7:Eu^{2+},Mn^{2+}$. The incorporated strength rises as the Y^{3+} ion level rises, showing that $Ca_8MgY(PO_4)_7$ could become a superior phosphor's host (Kang *et al.*, 2020).

$$Ca_{8-y}Mg_{1-z}Y(PO_4)_7{:}\,yEu^{2+},zMn^{2+}$$

The CaMg:EM has a PLE spectrum consisting of one wide line under the range between 250 and 450 nm, a result of the $4f^7$ ($^8S_{7/2}$) - $4f^65d^1$ permitted conversion in the ions of Eu^{2+}, showing that CaMg:EM becomes activated via the emitting illumination from several ultraviolet or close ultraviolet chips.

The experiential equation below, based on Van Uitert, gives an effective match to the emitting maximum for Eu^{2+} and Ce^{3+}. This equation can be used to analyze the crystal structure of the host lattice (Liu *et al.*, 2020):

$$E = Q\left[1 - \left(\frac{V}{4}\right)^{\frac{1}{V}} 10^{-\frac{nE_ar}{80}}\right] \quad (3)$$

E indicates the energy location for the rim of the d-band in the rare earth ion (measured via cm^{-1}). Q indicates the energy location for the lower rim of the d-band in free ions (measured via cm^{-1}). V indicates the trigger's valence. n indicates the anion amount within the trigger's surrounding exterior. r indicates the host cation's radius replaced with the trigger (measured via Å). E_a indicates the electron association for the atoms establishing anion (measured via eV). For this situation, we have a Q value of 34000 cm^{-1}, V value of 2, along with E_a value of 2.19 eV. By employing the said numbers for formula 3, the Eu^{2+} discharge peak may be calculated.

Generally, if the radiative transfer of energy works, the sensitizer decay period stays unchanged with or without a trigger. It is possible to calculate the lifetime duration using the equation as follows (Nabavi and Yuksel, 2020):

$$\tau * = \frac{A_1{\tau_1}^2 + A_2{\tau_2}^2 + A_3{\tau_3}^2}{A_1\tau_1 + A_2\tau_2 + A_3\tau_3} \quad (4)$$

In our situation, judging the average degradation period of the sensitizer lowered steadily alongside rising activator concentration, from 1247.98 ns to 777.00 ns, indicating non-radioactive power conversion among Eu^{2+} and Mn^{2+} as the ions of Mn^{2+} take in the power from Eu^{2+} prior to exponential damping. The absorptivity grows in severity as the content of the ions of Mn^{2+} increases. It is possible to assess the power shift performance between Eu^{2+} and Mn^{2+} using the given equation (Xu *et al.*, 2019):

$$\eta_T = 1 - \frac{\tau_s}{\tau_{so}} \quad (5)$$

τ_{so} and τ_s indicate the degradation periods for the ions of Eu^{2+} with or without the ions of Mn^{2+}, respectively. It can be shown that the T rises steadily as the Mn^{2+}-doping concentration rises, eventually reaching 0.377 at z = 0.21. The shift of energy from Eu^{2+} to Mn^{2+} appears to be relatively effective based on the reducing decay period and the rising value of T noted earlier in this section, the overlap among the PLE spectrum in Mn^{2+}, the PL spectrum of Eu^{2+}, as well as the reducing strength in Eu^{2+} under rising Mn^{2+} content described.

If the exchange interaction works, the formula below will be fitted linearly (Zhang and Yang, 2019):

$$ln\frac{\eta_{so}}{\eta_s}\alpha C \tag{6}$$

C represents the full content for the ions of Eu^{2+} as well as Mn^{2+}. η_{so} and η_s represent the luminescent quantum performance for Eu^{2+} with or without Mn^{2+}. The corresponding ratio of degradation period (τ_{so}/τ_s) may become useful for approximating the value of η_{so}/η_s.[26] As a result, equation 6 can be stated as follows (Sun *et al.*, 2019):

$$ln\frac{\tau_{so}}{\tau_s}\alpha C \tag{7}$$

The exchange interaction does not produce a linear relationship (R^2 = 0.947). As a result of the multiple-multiple interaction, the energy of Eu^{2+} is transferred to Mn^{2+}. The following relation can be established for multipolar interactions (Zhao *et al.*, 2021):

$$\frac{\eta_{so}}{\eta_s}\alpha C^{\alpha/3} \tag{8}$$

As previously stated, it is possible to express the formula above with another formula:

$$\frac{\tau_{so}}{\tau_s}\alpha C^{\alpha/3} \tag{9}$$

α denote dipole-dipole, dipole-quadrupole, and quadrupole-quadrupole interactivities, which assume respective values of 6, 8, and 10. It can be seen that a well-fitting linear relationship was found when α value is 8. Therefore, the dipole-quadrupole interactivity may be the major characteristic of the power shift between Eu^{2+} and Mn^{2+}.

The spectral overlap approach is used to measure the critical distance of energy conversion:

$$R_c{}^8 = 3.024 \times 10^{12}\lambda_s^2 f_q \int \frac{F_S(E)F_A(E)dE}{E^4} \tag{10}$$

f_q represents the oscillator potency for the trigger (which is 10−10 for Mn^{2+}). s indicates the wavelength location for the discharge of sensitizers (Eu^{2+}) (measured via Å). E indicates the power related to the shift (measured via eV). $/F_S(E)F_A(E)dE/E^4$ indicates the normalized spectrum overlay among the Eu^{2+} discharge $F_S(E)$. The Mn^{2+} excitation $F_A(E)$ assumed a value of 0.0340 $(eV)^{-5}$. As a result, the critical range in the case of dipole-quadrupole power transmission would be 11.17 Å.

In order to illustrate the possible usage of CaMg:EM phosphor, we created a LED device made of transmuting phosphor via creating a merger between one ultraviolet chip under 375 nm and CaMg:EM in white powered by a forward-bias current of 0.02 A. The white LED's CIE hue coordinate along with the corresponding hue temperature are (0.337, 0.334) and 5278 K, respectively. Prevention of UV light seeping out is vital when it comes to the

preservation of our safety as well as packaging resins. In addition, the spectrum of EL exhibits a small strength for the ultraviolet chip, indicating that CaMg:Em possesses strong absorptivity towards ultraviolet illumination as well as fulfilling the criteria of safety due to the particularly small ultraviolet discharge intensity, unlike earlier studies.

Figure 1 is the illustration showing the influence of CaMg:EM green phosphor on the concentration of YAG:Ce^{3+}. As shown, the green phosphor content grew from 2% to 20%, resulting in a decrease in yellow-phosphor content. This opposition means retaining average CCT levels and changing the illuminating scattering and absorbing factors for WLED devices with a pair of phosphor sheets. When the scattering and absorbing activities are influenced, the luminescence and color production of WLEDs can be modified and enhanced.

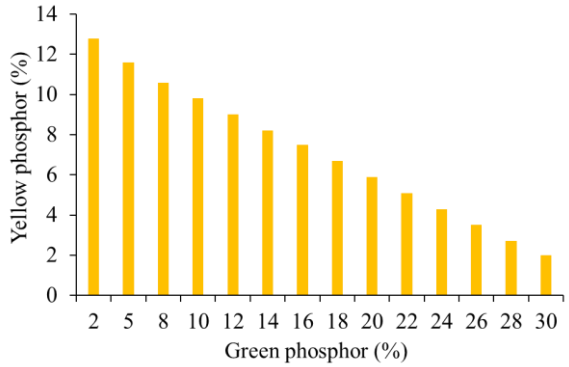

Figure 1 Altering phosphor content for the task of retaining median CCT values

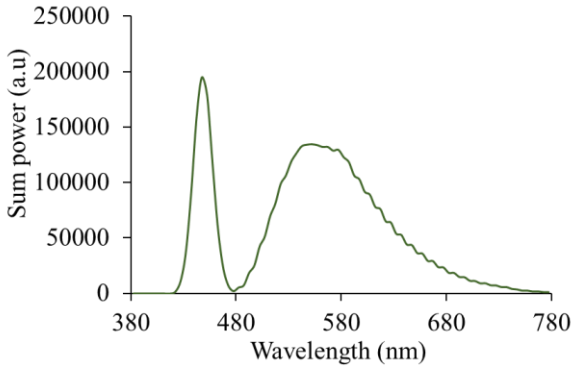

Figure 2 The discharge spectra in 5000-K WLED device correlating with CaMg:EM doping percentage

Figure 2 depicts the influence caused by CaMg:EM concentration on the emission power in the WLED device. By judging the production demands, we can pick an appropriate option. The WLED devices demanding good hue quality would slightly decrease illumination. From the line graph in Figure 2, the peak spectral power values are located at ~450 nm and 550-600 nm. Besides, the wide-band wavelength of 500 nm - 640 nm is also presented in this figure. These two findings suggest that the presence of CaMg:EM phosphor helps increase the illumination intensity of the WLED, especially for the blue (450 nm) and green-yellow (550-600 nm) spectral regions. The wide-band of 500 nm - 640 nm additionally indicates the addition of orange spectral energy to the white-illumination wavelength, thus, the color performance can be improved. Moreover, the rise of emission power implies that the blue-illumination dispersion and transmission are better with the addition of green phosphor CaMg:EM. Thus, the lumen output of the WLED when varying CaMg:EM concentration is presented to examine this state, as shown in Figure 3. The graph

points out that the light ray emitted rises dramatically when CaMg:EM content rises from 2% to 20%.

The hue divergence was considerably reduced alongside CaMg:EM content under every CCT value, shown by the results from Figure 4. This can be explained by the green phosphor layer's absorption. When CaMg:EM green phosphor takes in LED-chip blue illumination, it changes the blue lighting into green lighting. The CaMg:EM granules will take in yellow light as well. On the other hand, due to the absorptivity qualities in the material, the blue-illumination absorption would be greater than that of the phosphor-emitted yellow illumination. As a result, the increasing CaMg:EM amount boots the presence of green light energy in the WLED, and as such, the hue consistency is augmented. Color uniformity (lower hue-divergence level) is one of the critical features of today's WLED devices. Obviously, if hue consistency rises, the cost of WLED will rise as well. The advantage of employing CaMg:EM is its inexpensive cost. CaMg:EM can therefore be widely employed.

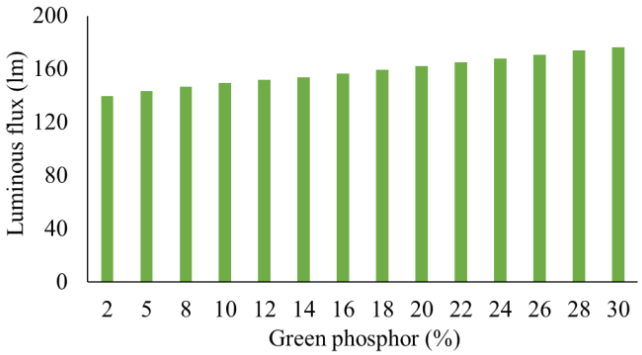

Figure 3 The luminous flux in WLED device correlating with CaMg:EM doping percentage

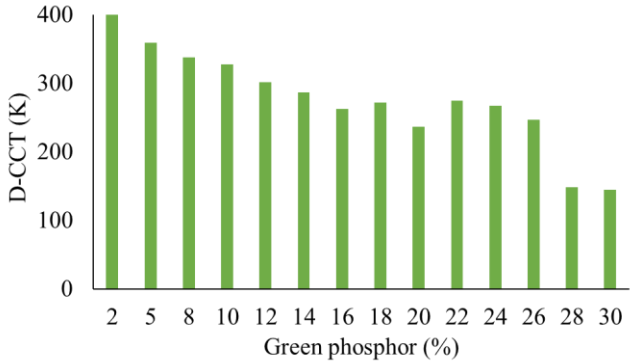

Figure 4 The color deviation in WLED device correlating with CaMg:EM doping percentage

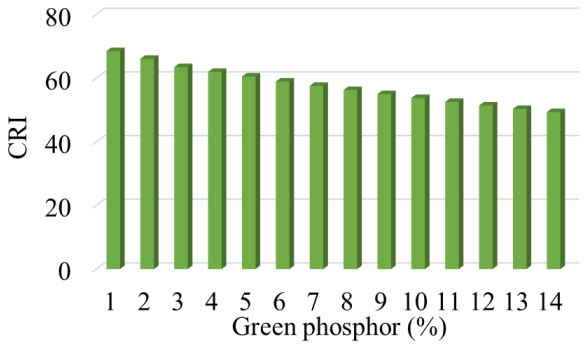

Figure 5 The color rendering indices (CRI) in WLED device correlating with CaMg:EM doping percentage

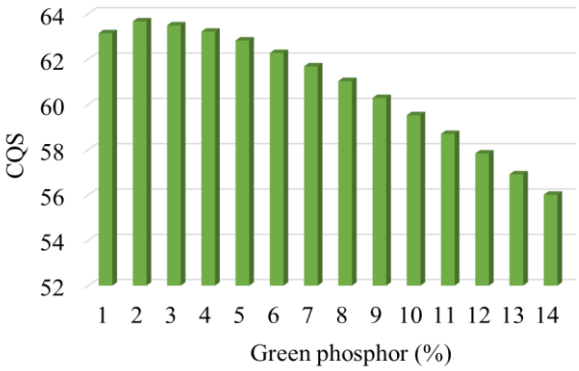

Figure 6 The color quality scales (CQS) in WLED device correlating with CaMg:EM doping percentage

In addition to the hue homogeneity, CRI and CQS are other important metrics for the color production of WLED light. Significant CRI alone does not define hue quality. As a result, subsequent studies provide a CRI as well as CQS. If light shines on the CRI, it determines the entity's real hue. The color imbalance will be generated by a surplus of green lighting hue over other crucial hues of blue and yellow, which notably decreases the WLED light's color fidelity (Li *et al*., 2020; Guo and Chi, 2020). Figure 5 shows the CRI performance regarding the varied concentration of CaMg:EM green phosphor, in which the CRI reduction is noticed as CaMg:EM doping percentage increases. On the other hand, such drawbacks would still be acceptable. When comparing CRI to CQS, the latter is much more important. It would be determined via CRI, the chromatic coordinates, and the viewer's visual preferences; so, CQS proves to be a better metric to access white-light color quality evaluation and enhancement. Figure 6 exhibits a CQS boost with the presence of the remote CaMg:EM layer. Furthermore, when the CaMg:EM concentration is raised, CQS does not alter considerably with CaMg:EM concentrations less than 10% wt. When the CaMg:EM doping percentage surpasses 10% wt., significant degradation in CQS and CRI is observed, which is caused by the mentioned surplus in green illumination. If CaMg:EM is employed, proper concentration selection would be necessary.

4. Conclusions

In conclusion, we used the solid-state technique under significant temperatures to create multiple $Ca_8MgLa(PO_4)_7:Eu^{2+}$ as well as $Ca_8MgY(PO_4)_7:Eu^{2+},Mn^{2+}$ phosphors. The luminescence in $Ca_8MgLa(PO_4)_7:Eu^{2+}$ suggests that it possesses one major promising applicability when it comes to WLED devices with three hues along with various applications. Furthermore, we exhibited the process of ions of Eu^{2+} replacing three distinct locations of Ca^{2+} within $Ca_8MgY(PO_4)_7$ using crystal formation data, the Gaussian Deconvolution technique, Van Uitert's hypothetical computation, along with degradation period. More significantly, adjusting the Mn^{2+} level in the phosphor resulted in color-adjustable CaMg:EM ranging between cyan (0.216, 0.352), white (0.330, 0.328), and finally pale red (0.370, 0.320). In addition, we studied the power transmission among Eu^{2+} as well as Mn^{2+}, then concluded that it was resonant through dipole-quadrupole interactivity having a threshold range measured at 11.17 Å. Eventually, one WLED apparatus made using a 375 nm ultraviolet chip as well as CaMg:EM produces illumination in white yielding one CIE shown as (0.337, 0.334) as well as corresponding hue temperature measured at 5278 K. As a result, CaMg:EM may be useful for phosphor-converted white LEDs. According to our findings, more optimization studies may be conducted for the task of acquiring superior

photoluminescent features for $Ca_8MgLa(PO_4)_7:Eu^{2+}$ as well as $Ca_8MgY(PO_4)_7:Eu^{2+},Mn^{2+}$ using different processes including hydrothermal as well as sol-gel methods. Additionally, the drop near the wavelength region of 550 nm where our sight possesses the greatest responsiveness would be one frequent flaw from phosphors treated with a pair of Eu^{2+} and Mn^{2+} as well as Ce^{3+} and Mn^{2+}.[27] The technique that involves doping ions of Tb^{3+} as well as altering the content for ions of Eu^{2+},Tb^{3+}, as well as Mn^{2+} is predicted to overcome this issue.

Acknowledgments

This research is supported by Industrial University of Ho Chi Minh City (IUH) under grant number 138/HD-DHCN.

References

Adnan, A., Liu, Y., Chow, C., Yeh, C., 2020. Demonstration of Non-Hermitian Symmetry (NHS) Serial-Complex-Valued Orthogonal Frequency Division Multiplexing (SCV-OFDM) for White-Light Visible Light Communication (VLC). *OSA Continuum*, Volume 3(5), pp. 1163–1168

Chen, J., Tang, Y., Yi, X., Tian, Y., Ao, G., Hao, D., Lin, Y., Zhou, S., 2019a. Fabrication of $(Tb,Gd)_3Al_5O_{12}:Ce^{3+}$ Phosphor Ceramics For Warm White Light-Emitting Diodes Application. *Optical Materials Express*, Volume 9(8), pp. 3333–3341

Chen, J., Fritz, B., Liang, G., Ding, X., Lemmer, U., Gomard, G., 2019b. Microlens Arrays with Adjustable Aspect Ratio Fabricated by Electrowetting and Their Application to Correlated Color Temperature Tunable Light-Emitting Diodes. *Optics Express*, Volume 27(4), pp. A25–A38

Dang, R., Tan, H., Wang, N., Liu, G., Zhang, F., Song, X., 2020. Raman Spectroscopy-Based Method for Evaluating LED Illumination-Induced Damage to Pigments in High-Light-Sensitivity Art. *Applied Optics*, Volume 59(15), pp. 4599–4605

Guo X., Chi, N., 2019. Superposed 32QAM Constellation Design for 2 × 2 Spatial Multiplexing MIMO VLC Systems. *Journal of Lightwave Technology*, Volume 38(7), pp. 1702–1711

Hakim, F.N., Muhamadinah, Y., Atthaillah, A., Mangkuto, R.A., Sudarsono, A.S., 2021. Building Envelope Design Optimization of a Hypothetical Classroom Considering Energy Consumption, Daylighting, and Thermal Comfort: Case Study in Lhokseumawe, Indonesia. *International Journal of Technology*, Volume 12(6), pp. 1217–1227

Huu, P.D., Thi, D.A.N., 2022. Selection of Multi-Layer Remote Phosphor Structure for Heightened Chromaticity and Luminous Performance of White Light-Emitting Diodes. *International Journal of Technology*, Volume 13(4), pp. 837–847

Jen, Y., Lee, X., Lin, S., Sun, C., Wu, C., Yu, Y., Yang, T., 2019. Design of an Energy-Efficient Marine Signal Light Based on White LEDs. *OSA Continuum*, Volume 2(8), pp. 2460–2469

Kang, T.W., Lee, S., Park, Y.J., Jeong, G.J., Kim, J.S., Bae, B., Hwang, J., Kim, S.W., 2020. Enhancement of The Optical Properties of $CsPbBr_3$ Perovskite Nanocrystals Using Three Different Solvents. *Optics Letters*, Volume 45(18), pp. 4972–4975

Kaur, P., Kaur, S., Kandasami, A., Singh, D.P., 2020. Synchrotron-Based VUV excitation-Induced Ultrahigh Quality Cool White Light Luminescence from Sm-Doped ZnO. *Optics Letters*, Volume 45(12), pp. 3349–3352

Kim, C.S., Kim, W., Lee, K., Yoo, H., 2019. High-Speed Color Three-Dimensional Measurement Based on Parallel Confocal Detection with a Focus Tunable Lens. *Optics Express*, Volume 27(20), pp. 28466–28479

Kumar, S., Mahadevappa, M., Dutta, P.K., 2019. Extended Light-Source-Based Lensless Microscopy Using Constrained and Regularized Reconstruction. *Applied Optics*, Volume 58(3), pp. 509–516

Li, J., Han, D., Zeng, J., Deng, J., Hu, N., Yang, J., 2020. Multi-Channel Surface Plasmon Resonance Biosensor Using Prism-Based Wavelength Interrogation. *Optics Express*, Volume 28(9), pp. 14007–14017

Lin, C., Verma, A., Kang, C., Pai, Y., Chen, T., Yang, J., Sher, C., Yang, Y., Lee, P., Lin, C., Wu, Y., Sharma, S.K., Wu, T., Chung, S., Kuo, H., 2019. Hybrid-Type White LEDs Based on Inorganic Halide Perovskite QDs: Candidates for Wide Color Gamut Display Backlights. *Photonics Research*, Volume 7(5), pp. 579–585

Liu, X., Li, J., Li, J., Huang, Z., 2020. Analysis of The Single-FFT Receiver for Layered ACO-OFDM in Visible Light Communications. *Journal of Lightwave Technology*, Volume 38(17), pp. 4757–4764

Liu, P., Guan, Z., Zhou, T., Xie, Q., Yu, Q., He, Y., Zeng, Z., Wang, X., 2021. Laser Regulation for Variable Color Temperature Lighting with Low Energy Consumption by Microlens Arrays. *Applied Optics*, Volume 60(19), pp. 5652–5661

Nabavi, P., Yuksel, M., 2020. Comprehensive Design and Prototype of VLC Receivers with Large Detection Areas. *Journal Lightwave Technology*, Volume 38(16), pp. 4187–4204

Orudzhev, T.Y., Abdullaeva, S.G., Dzhabbarov, R.B., 2019. Increasing The Extraction Efficiency of a Light-Emitting Diode Using a Pyramid-Like Phosphor Layer. *Journal of Optical Technology,* Volume 86(10), pp. 671–676

Sun, Y., Zhang, C., Yang, Y., Ma, H., Sun, Y., 2019. Improving The Color Gamut of A Liquid-Crystal Display by Using a Bandpass Filter. *Current Optics and Photonics*, Volume 3(6), pp. 590–596

Sun, C.C., You, A.H., Teo, L.L., 2022. XRD Measurement for Particle Size Analysis of PMMA Polymer Electrolytes with SiO2. *International Journal of Technology*, Volume 13(6), pp. 1336–1343

Xia, G., Ma, Y., Chen, X., Jin, S.Q., Huang, C., 2019. Comparison of MAP Method with Classical Methods for Bandpass Correction of White LED Spectra. *Journal of the Optical Society of America*, Volume 36(5), pp. 751–758

Xu, B., Wu, Q., Bao, Y., Chen, G., Wang, Y., Ren, S., 2019. Time-Multiplexed Stereoscopic Display with a Quantum Dot-Polymer Scanning Backlight. *Applied Optics*, Volume 58(16), pp. 4526–4532

Yigen, S., Ekmekcioglu, M., Ozdemir, M., Aygun, G., Ozyuzer, L., 2021. Compact Multilayer Thin-Film Color Filters and Direct Integration on White-Light-Emitting Diodes for Color Conversion. *Applied Optics*, Volume 60(28), pp. 8949–8955

Yu, B., Liang, S., Zhang, F., Li, Z., Liu, B., Ding, X., 2021. Water-Stable CsPbBr3 Perovskite Quantum-Dot Luminous Fibers Fabricated by Centrifugal Spinning for Dual White Light Illumination and Communication. *Photonics Research*, Volume 9(8), pp. 1559–1568

Zhang Z., Yang, W., 2019. Tunable Photoluminescence in Ba1-Xsrxsi$_3$o$_4$n$_2$: Eu^{2+}/ Ce^{3+}, Li^{+} Solid Solution Phosphors Induced by Linear Structural Evolution. *Optical Materials Express,* Volume 9(4), pp. 1922–1932

Zhao, S., Mo, Q., Cai, W., Wang, H., Zang, Z., 2021. Inorganic Lead-Free Cesium Copper Chlorine Nanocrystal for Highly Efficient and Stable Warm White Light-Emitting Diodes. *Photonics Research*, Volume 9(2), pp. 187–192